Large anomalous Hall and Nernst effects in the ferromagnetic semimetal candidate Mn_3Sn_2

Jianli Bai [1,2] Qingxin Dong,[1,2] Binbin Ruan,[1] Libo Zhang,[1,2] Qiaoyu Liu,[1,2] Jingwen Cheng,[1,2] Pinyu Liu,[1,2] Cundong Li,[1,2] Yingrui Sun,[1,2] Yu Huang,[1,2] Zhian Ren,[1,2] and Genfu Chen[1,2,3,*]

[1] *Institute of Physics and Beijing National Laboratory for Condensed Matter Physics, Chinese Academy of Sciences, Beijing 100190, China*

[2] *School of Physical Sciences, University of Chinese Academy of Sciences, Beijing 100049, China*

[3] *Songshan Lake Materials Laboratory, Dongguan, Guangdong 523808, China*

(Received 3 November 2023; revised 3 February 2024; accepted 20 February 2024; published 8 March 2024)

Recent theoretical calculations have shown that Mn_3Sn_2, a well-known magnetocaloric material with multiple magnetic transitions, possesses both nodal lines and nodal surfaces in its electronic structures, making it an excellent platform for studying anomalous transport properties in magnetic topological candidates. In this work, we performed comprehensive electrical, thermal, and thermoelectric measurements on Mn_3Sn_2 single crystals. The electrical resistivity $\rho(T)$ shows an abnormal peak near the Curie temperature, $T_{C2} \sim 227$ K, and a negative resistivity slope above T_{C2}, which are probably related to a large spin-fluctuation scattering. The Seebeck coefficient $S_{xx}(T)$ shows a sign reversal below 80 K although the Hall coefficient is always positive, which might be ascribed to the magnon-drag effect. Below $T_{C1} \sim 262$ K, a significant anomalous Hall effect is observed, and the anomalous Hall resistance (ρ^A_{xy}) peaks at around 7 $\mu\Omega$ cm at 200 K. ρ^A_{xy} exhibits a quadratic dependence on the longitudinal resistivity ρ_{xx}, and the anomalous Hall conductivity σ^A_{xy} remains nearly temperature independent below 200 K, suggesting the dominance of the intrinsic Berry-phase mechanism. Correspondingly, we also detect a large anomalous Nernst effect, with the anomalous Nernst coefficient reaching approximately 1 μV K^{-1} at 200 K. Despite Mn_3Sn_2 exhibiting robust ferromagnetism, its anomalous Hall angle (2.5%), anomalous Nernst angle (6.5%), and large anomalous Nernst coefficient (1.65 μV K^{-1} T^{-1}) surpass those observed in typical ferromagnetic materials. Our results experimentally demonstrate the existence of topologically nontrivial states in Mn_3Sn_2.

DOI: 10.1103/PhysRevB.109.125112

I. INTRODUCTION

The ordinary Hall effect (OHE), referring to the transverse electric field generated by a longitudinal charge current in the presence of a magnetic field, is caused by the Lorentz force exerted on charge carriers by the magnetic field. In ferromagnetic solids, there is an additional component to this effect, commonly known as the anomalous Hall effect (AHE), typically believed to arise from a substantial magnetization. Since its discovery more than a century ago [1], the AHE has been extensively studied both theoretically and experimentally, due to its fundamental physics and significant potential applications [2]. Similarly, the generation of an additional electric voltage orthogonal to the applied temperature gradient due to the internal magnetization is referred to as the anomalous Nernst effect (ANE), serving as the thermoelectric counterpart of the AHE. In contrast to the Seebeck effect, the ANE has been much less explored to date [3]. Due to the transverse nature of the Nernst effect and its dependency on the temperature gradient, rather than the temperature difference, the Nernst device exhibits superior conversion efficiency compared to the Seebeck device, given an identical figure of merit. Additionally, the Nernst voltage remains unaffected by the Ettingshausen heat current, in contrast to the potential negative impact of the Peltier heat current on the Seebeck voltage. Consequently, a thermoelectric conversion module utilizing the Nernst effect experiences greater design flexibility [4].

It is generally believed that the intrinsic origin of the AHE and the ANE is closely related to the quantal Berry phase of Bloch electrons [5], and can be significantly enhanced when the Weyl points are tuned to be close enough to the Fermi energy [2,4,6]. For instance, giant ANEs have been observed in ferromagnetic Dirac and Weyl semimetals, such as $Co_3Sn_2S_2$ [7] and Co_2MnGa [8]. Specifically, a large AHE and a spontaneous Hall effect have been detected in Mn_3Sn, a noncollinear antiferromagnet with a small magnetization [9], and $Pr_2Ir_2O_7$, a spin liquid compound without spin magnetization [10], respectively. The intrinsic part of the AHE is determined by integrating the Berry curvature for all the occupied bands, while the ANE is determined by the Berry curvature of bands located at E_F, providing an effective probe of the topological nature of materials [5,11].

Recently, we successfully grew the Mn_3Sn_2 single crystal [12]. This compound is a promising magnetocaloric material with great potential for applications in low temperature refrigeration [12,13]. Mn_3Sn_2 crystalizes in the Ni_3Sn_2-type (*Pnma*) structure and undergoes two successive ferromagnetic transitions at ∼262 K and ∼227 K, followed by an antiferromagnetic transition at ∼192 K, as illustrated in Figs. 1(a) and 1(b). As reported in our previous work, significant anisotropy of magnetic susceptibility and multiple field-induced metamagnetic transitions were found at low fields in Mn_3Sn_2 single crystals [12]. The maximum of magnetic entropy change

*gfchen@iphy.ac.cn

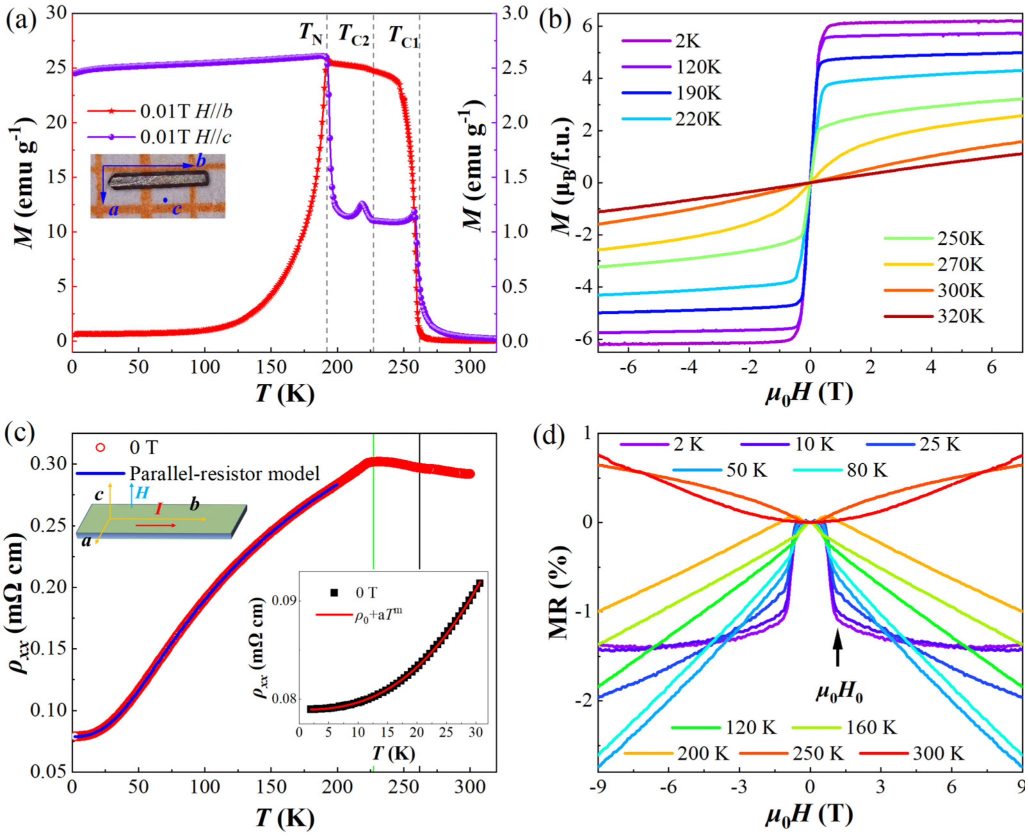

FIG. 1. (a) Temperature-dependent magnetization of Mn_3Sn_2 measured in the zero-field-cooling mode at $\mu_0 H = 0.01$ T, with H parallel to b and c axis, respectively. The dotted lines indicate the positions of the magnetic phase transitions. The inset shows the optical image of a single crystal sample with respect to the crystalline axes on a millimeter grid. (b) Magnetic field dependent magnetization measured with H // c under various temperatures. (c) Temperature dependence of ρ_{xx} without a magnetic field. The vertical lines show the positions of the two ferromagnetic transitions. The right inset presents the results of fitting the low temperature resistance with equation $\rho_{xx}(T) = \rho_0 + aT^m$. The left inset shows the contact configuration for measuring the electrical transport properties. A small kink is observed at $T_{C1} \sim 262$ K where the resistivity increases faster and the maximum appears at $T_{C2} \sim 227$ K, corresponding to the two ferromagnetic transitions while no anomaly is visible at T_N. (d) The magnetic field dependent magnetoresistance measured under selected temperatures with H parallel to c axis and the current I parallel to b axis.

reaches approximately 4.01 J kg^{-1} K^{-1} under a magnetic field change of 5 T, accompanied by a corresponding refrigerant capacity of 1750 mJ cm^{-3}. Remarkably, recent theoretical calculations suggest that Mn_3Sn_2 might be a novel magnetic topological material, characterized by the coexistence of essential nodal lines and nodal surfaces [14]. Analogous to the Weyl node, both nodal lines and nodal surfaces can generate a finite Berry curvature, resulting in anomalous velocity and giving rise to the AHE and ANE. Ternary Heusler compounds, formulated as X_2YZ (where X and Y are transition metals and Z is a main group element), have been extensively investigated due to their nodal line band structure [15–17]. For example, giant AHE and the largest ANE were observed in the famous ferromagnetic Heusler compound Co_2MnGa [8]. The largest anomalous Hall angle was observed in the ferromagnetic kagome-lattice nodal line semimetal $Co_3Sn_2S_2$ [18]. Both large anomalous Hall angle and anomalous Nernst angle were reported in nodal line semimetal Fe_3GeTe_2 [19]. Although the nodal surface has more advantages in contributing to the effective energy integral paths and enhancing Berry curvature [20], the formation of such a nontrivial nodal plane near the Fermi level has rarely been studied to date.

In this study, we performed magnetoelectrical, thermal, and thermoelectric measurements on Mn_3Sn_2 single crystals. Significant anomalous Hall and Nernst responses were observed. The anomalous Hall resistivity ρ^A_{xy} reaches approximately 7 $\mu\Omega$ cm at 200 K and exhibits quadratic scaling behavior with respect to ρ_{xx}, which suggests that the primary contribution to the observed AHE stems from the intrinsic Karplus and Luttinger (KL) mechanism. A jump of $\sim$1 μV K^{-1} in the Nernst effect around zero field at 200 K indicates the significant role of occupied bands near E_F in the anomalous transport properties. The corresponding remarkable anomalous Nernst coefficient ($\sim$1.65 μV K^{-1} T^{-1}) and a large anomalous Nernst angle ($\sim$6.5%) are unexpected based on conventional scaling law with magnetization. Our findings provide experimental evidence for the existence of topologically nontrivial states in Mn_3Sn_2, aligning with the proposal [14].

II. EXPERIMENTAL METHODS

Single crystals of Mn_3Sn_2 were grown from Bi flux as previously reported by our group [12]. The determined lattice parameters are $a = 6.344$ Å, $b = 3.450$ Å, and $c = 8.586$ Å, respectively. As shown in the inset of Fig. 1(a), the obtained single crystals are of a strip shape of about 2 mm length, and the relationship between single-crystal geometrical surfaces and crystallographic axes is also depicted. The residual Bi flux was etched away from the crystalline facets in diluted HNO_3 before measuring. Thermal, electrical, and thermoelectric transport measurements on Mn_3Sn_2 single crystals were performed on a Quantum Design physical property measurement system (PPMS). Thermal conductivity, Seebeck coefficient, and Nernst coefficient measurements were performed using a steady-state thermal measurement method. Two pairs of calibrated thin $AuFe_{0.07\%}$-chromel thermocouple were used to detect the thermal gradient across the samples. A resistance chip served as a heater to generate a heat current. Voltage values of thermocouple between the hot and cold terminals, as well as Seebeck and Nernst signals, were detected using Keithley 2182A nanovoltmeters. Magnetic properties were characterized by a Quantum Design vibrating sample magnetometer (VSM).

III. RESULTS AND DISCUSSION

A. Resistivity and magnetoresistance

To conduct the electrical and thermoelectric measurements, the crystal was oriented and cut into a bar. Figure 1(c) illustrates the temperature-dependent resistivity $\rho_{xx}(T)$ of Mn_3Sn_2 single crystal measured by the standard four-probe method at zero field, with a current ($I = 1$ mA) parallel to the b axis and a magnetic field (H) parallel to the c axis. With the temperature decreasing, $\rho_{xx}(T)$ increases and forms a maximum at T_{C2}. The more negative temperature coefficient indicates the presence of a large spin-fluctuation scattering in addition to the electron-phonon scattering in the paramagnetic state. Below T_{C2}, $\rho_{xx}(T)$ exhibits metallic behavior with a residual resistivity ratio [RRR $= \rho_{xx}(300\,\mathrm{K})/\rho_{xx}(2\,\mathrm{K})$] of approximately 3.8, comparable to that of Mn_3Sn [21]. Under the assumption of a spherical Fermi surface with one sheet (i.e., having only one band crossing the Fermi surface),

$$\rho = \frac{3\pi h}{2e^2 k_F^2 l}, \tag{1}$$

$$n = \frac{k_F^3}{3\pi^2}, \tag{2}$$

where k_F is the Fermi wave vector, l is the mean-free-path, and h is the Planck constant. Then, combining the carrier concentration derived from the Hall effect below, a resistivity of 284 $\mu\Omega\,$cm at 200 K suggests a mean-free path as short as 7.52 Å, which is comparable to the lattice constants ($b = 5.4946$ Å) of Mn_3Sn_2, and thus a resistivity saturation would be expected [22]. As the temperature decreases down to the Curie temperature T_{C2}, the spin-fluctuation scattering increases while electron-phonon scattering saturates, leading to a broad peak at T_{C2}. The blue line in Fig. 1(c) presents a simulation of the zero-field resistivity ranging 2–200 K using the Parallel-resistor model,

$$\frac{1}{\rho_{xx}(T)} = \frac{1}{\rho(T)} + \frac{1}{\rho_{sat}}, \tag{3}$$

$$\rho(T) = \rho(0) + A\left(\frac{T}{\Theta_R}\right)^n \int_0^{\Theta_R/T} \frac{t^n}{(e^t - 1)(1 - e^{-t})} dt, \tag{4}$$

where $\rho(T)$ represents the temperature-dependent contribution expressed by the Bloch-Gruneisen formula [23,24], and ρ_{sat} is the temperature-independent saturation resistivity. In Eq. (4), $\rho(0)$ is the residual resistivity due to scattering, which is essentially temperature independent. A is a constant with varying values for different metals, Θ_R is a characteristic temperature closely aligned with the Debye temperature Θ_D obtained from specific heat measurements, and n is an integer dependent on the nature of the interaction. This fitting yields $\rho(0) = 0.092$ m$\Omega\,$cm, $\rho_{sat} = 0.55$ m$\Omega\,$cm, $A = 1.15$ m$\Omega\,$cm, $n = 2.4$, and $\Theta_R = 315$ K. $n = 2.4$ instead of an integer (2, 3, and 5) indicates that the resistivity behavior of Mn_3Sn_2 cannot be simply described by electron-electron or electron-phonon scattering mechanisms. As shown in the right inset of Fig. 1(c), a power law fit was also performed for $\rho_{xx}(T)$ at low temperature using the equation $\rho_{xx}(T) = \rho_0 + aT^m$. Here, $m = 2.6$ indicates a deviation from Fermi liquid behavior in the ground state, likely resulting from a combination of electron-electron and electron-magnon interactions.

Figure 1(d) shows the field-dependent magnetoresistance ($MR = \frac{\rho(\mu_0 H) - \rho(0)}{\rho(0)} \times 100\%$) at different temperatures with $\mu_0 H$ (up to 9 T) parallel to the c axis and I parallel to the b axis. Negative MR, resulting from the suppression of spin scattering, is observed at temperatures below T_N. The change in MR slows down at the characteristic magnetic field $\mu_0 H_0$, corresponding to the saturated magnetic field in the magnetization curve, at which further increasing of the field will have a much weaker influence on the alignment of spins. In the temperature range 190–230 K, the MR is positive up to the saturated field and becomes negative at higher fields. The positive MR occurs because the low magnetic field is not sufficient to shift the magnetic moment from the b axis to the c axis, countering the effect of Lorentzian deflection. At higher temperatures, the MR increases with the rising magnetic field. The increasing speed slows down at $T_{C1} < T < T_{C2}$ and gradually accelerates at $T > T_{C2}$. The positive MR should originate from the Lorenz force caused by a magnetic field on the carrier motion, although it is also influenced by the ferromagnetic order below T_{C1}.

B. Hall effect

Additionally, we have performed Hall-effect measurements on the single crystals of Mn_3Sn_2 at various temperatures. To eliminate the longitudinal resistivity contribution arising from voltage probe misalignment, we derived the Hall resistivity ρ_{xy} as the difference in transverse resistance measured at positive and negative fields, expressed as $\rho(\mu_0 H) = [\rho(+\mu_0 H) - \rho(-\mu_0 H)]/2$. Figure 2(a) illustrates the magnetic field dependence of $\rho_{xy}(\mu_0 H)$ at selected temperatures from 2 to 300 K. Over the entire temperature range, $\rho_{xy}(\mu_0 H)$ exhibits a positive slope, indicating the dominance of hole-type carriers in the transport process. In the low-field range, ρ_{xy} strongly reflects $M(\mu_0 H)$—a characteristic of the AHE with a maximum at around 200 K. It decreases upon cooling, although the saturation magnetization increases. A similar trend was observed in the anomalous Nernst coefficient measured below. It is noteworthy that the saturated value of $\rho_{xy}(\mu_0 H)$ for the Mn_3Sn_2 single crystal at 200 K is enormous

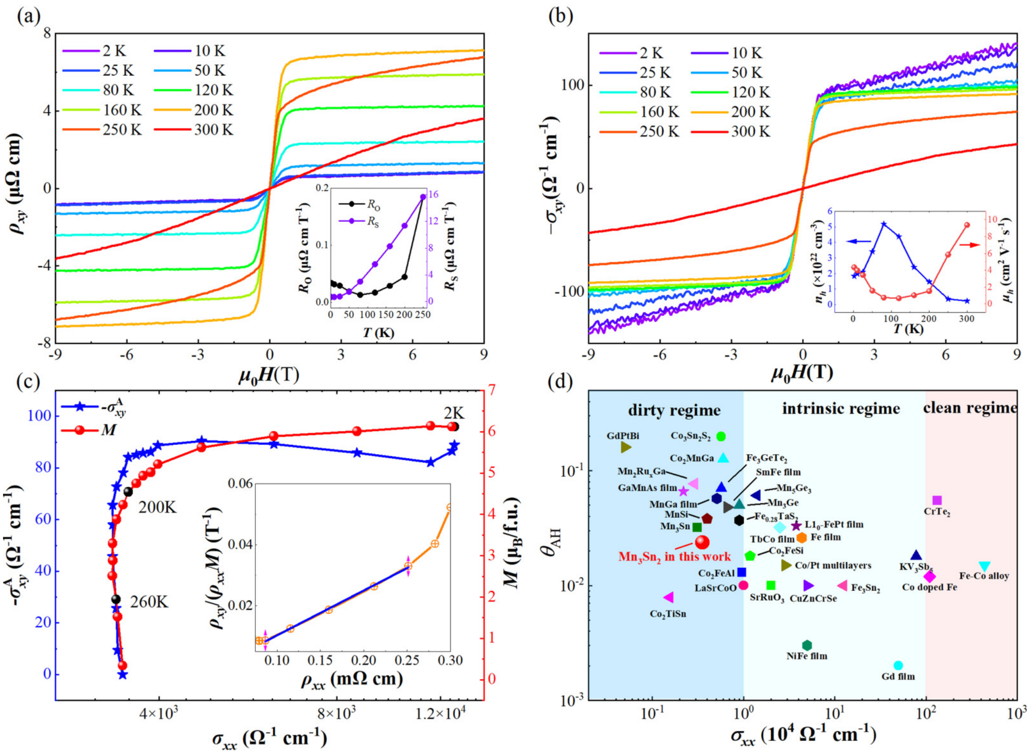

FIG. 2. (a) Magnetic field dependence of the Hall resistivity measured at selected temperatures with H parallel to c axis and the current I parallel to b axis. The inset shows the temperature dependence of both ordinary and anomalous Hall coefficients. (b) Magnetic field dependence of Hall conductivity σ_{xx}. The inset presents the extracted carrier density n_h and mobility μ_h using a one-band model. (c) Plot of M and $-\sigma^A_{xy}$ versus σ_{xx}, here the temperature is an implicit parameter. The inset shows the plot of $-\rho^A_{xy}/M\rho_{xx}$ versus ρ_{xx} with the blue line indicating a linear fit to Eq. (7). (d) θ_{AH} vs σ_{xx} plot for Mn_3Sn_2 and other reported anomalous Hall materials. Except for Mn_3Sn_2, the data for other materials were extracted from Refs. [18,29–34].

($\sim$7 $\mu\Omega$ cm), surpassing those of typical itinerant ferromagnets like Fe, Co, and Ni [2,25–27]. It is comparable to Weyl antiferromagnet Mn_3Sn [9] and kagome ferromagnet Fe_3Sn_2 [28].

In ferromagnetic conductors, it is conventional to express $\rho_{xy}(\mu_0 H)$ in terms of contributions from the ordinary Hall coefficient (R_{O}) and the anomalous one (R_{S}): $\rho_{xy} = R_{\mathrm{O}}B + 4\pi R_{\mathrm{S}}M$ [2]. As shown in the inset of Fig. 2(a), R_{S} is significantly larger than R_{O} and about two orders of magnitude larger ($\sim$11.4 $\mu\Omega\,\mathrm{cm\,T^{-1}}$ at 200 K) than those of conventional itinerant ferromagnets at the same reduced temperature (T/T_{C}) [25]. At higher fields, ρ_{xy} exhibits nearly linear behavior, which can be fitted by a simple one-band model:

$$\rho_{xy} = R_H B = \frac{B}{n_h e}, \tag{5}$$

$$\mu_h = R_H \sigma_{xx}(0). \tag{6}$$

The extracted carrier density (n_h) and mobility (μ_h) are $1.8 \times 10^{22}\mathrm{cm^{-3}}$ and 4.3 $\mathrm{cm^2\,V^{-1}\,s^{-1}}$ at 2 K, as shown in the inset of Fig. 2(b), which is similar to that of semimetal Mn_3Sn [9], corresponding to about 1.6 carriers per formula unit of Mn_3Sn_2. An extreme value of n_h is observed around 80 K, and this anomaly as a function of temperature has been seen only in the carrier density and should not be related to magnetic transitions, which indicates a possible subtle change in the band structure.

To distinguish the intrinsic and extrinsic contributions to the AHE, we thus express it as

$$\rho^A_{xy} = a(M)\rho_{xx} + b(M)\rho^2_{xx}, \tag{7}$$

where the functions $a(M)$ and $b(M)$ generally depend on the magnetization. The skew scattering contribution $a(M)$ is usually linear in magnetization. As depicted in the inset of Fig. 2(c), a linear fit to the curve of $-\rho^A_{xy}/M\rho_{xx}$ vs ρ_{xx} yields an intercept $\frac{a(M)}{M} = 4.36 \times 10^{-3} T^{-1}$ and the slope $\frac{b(M)}{M} = 0.147\ T^{-1}\mathrm{m}\Omega^{-1}\,\mathrm{cm}^{-1}$. The full AHE usually consists of three components: intrinsic, skew scattering, and side-jump contributions. However, it is experimentally difficult to distinguish the extrinsic side-jump mechanism from the KL mechanism because they exhibit the same scalar relationship, $\rho^A_{xy} \propto \rho^2_{xx}$. From the theoretical viewpoint, the magnitude of σ_{xy} in the intrinsic regime is approximately 10^2–$10^3\Omega^{-1}\,\mathrm{cm}^{-1}$, while the side jump contribution should be much smaller by a factor of $E_{\mathrm{SO}}/E_{\mathrm{F}} \sim 10^{-3}$–$10^{-2}$, where E_{SO} is the spin-orbit interaction energy and E_{F} is the Fermi energy [27,35]. As discussed later, the value of the temperature independent σ^A_{xy} is closer to an intrinsic contribution one, thus it is primarily attributed to the KL mechanism. Consequently, the ratio of the intrinsic contribution to the extrinsic one, i.e., $b(M)\rho_{xx}/a(M) \approx 10$, suggests the primary contribution to the observed AHE originates from the intrinsic Berry-phase mechanism. We note that the first principle calculation is needed to further clarify the precise nature of the anomalous Hall effect in Mn_3Sn_2.

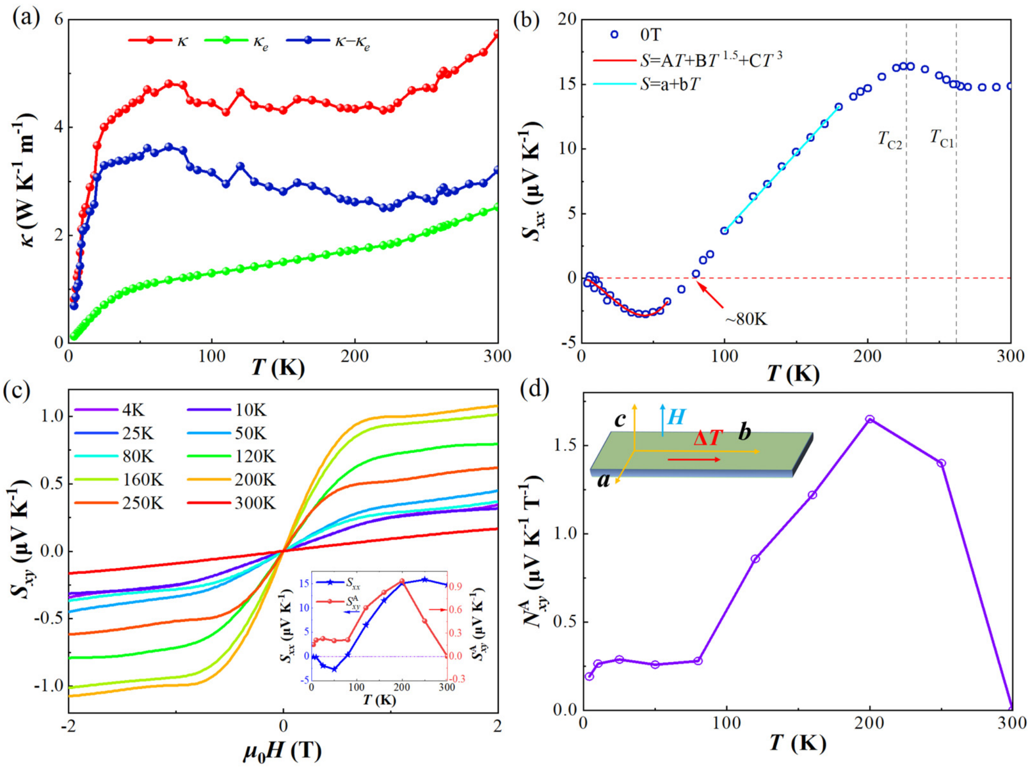

FIG. 3. (a) Temperature dependence of total thermal conductivity κ, electronic thermal conductivity κ_e, and lattice thermal conductivity $\kappa - \kappa_e$. (b) Plot of Seebeck coefficient S_{xx} versus T measured without an external field. The vertical dotted lines indicate the positions of the two ferromagnetic phase transitions and the red arrow marks the zero point of S_{xx}. (c) Magnetic field dependence of Nernst effect at selected temperatures. The inset shows the temperature dependence of anomalous Nernst effect and the corresponding S_{xx}. (d) The temperature dependence of the anomalous Nernst coefficient. The inset shows the contact configuration for measuring the thermal transport properties, i.e., the temperature gradient ΔT is parallel to b axis and H is parallel to c axis.

Figure 2(b) shows the magnetic field dependence of the longitudinal conductivity σ_{xx} and Hall conductivity σ_{xy}, calculated by

$$\sigma_{xx} = \frac{\rho_{xx}}{\rho_{xx}^2 + \rho_{xy}^2}, \quad (8)$$

$$\sigma_{xy} = \frac{-\rho_{xy}}{\rho_{xx}^2 + \rho_{xy}^2}. \quad (9)$$

The anomalous Hall conductivity σ_{xy}^A obtained by extrapolating the slope of the high-field data to the zero-field value remains almost constant and insensitive to σ_{xx} (or T) below 200 K, exhibiting a trend similar to M ($\sigma_{xy}^A \propto M$) throughout the experimental temperature range, as shown in Fig. 2(c). This scaling relationship suggests once again that the intrinsic Berry-phase mechanism dominates the AHE in Mn_3Sn_2 [2,36]. Combined with Fig. 2(d), Mn_3Sn_2 lies in the transition zone ($\sigma_{xx} \sim 10^4 \Omega^{-1}\,\text{cm}^{-1}$) between the dirty regime and the intrinsic regime. the medium-sized anomalous Hall angle ($\theta_{AH} = \sigma_{xy}^A/\sigma_{xx} \approx 0.025$) at 200 K is close to that of Mn_3Sn [9] and larger than those of most common ferromagnetic metals and alloys such as the Heusler compound Co_2TiSn [31].

C. Thermal and thermoelectric properties

Subsequently, we examined the thermal and thermoelectric transport properties of Mn_3Sn_2. The temperature-dependent thermal conduction κ exhibits a characteristic broad peak around $T = 50$ K, as illustrated in Fig. 3(a), which results from the competition between the umklapp phonon scattering dominating at high temperature and the phonon scattering by defects dominating at low temperature [37]. By subtracting the electronic thermal conductivity κ_e (calculated based on the Wiedemann-Franz law [38]) from κ, we observe that the combined contribution of phonons and magnons to the longitudinal thermal transport is comparable to that of electrons. The upturn in $\kappa - \kappa_e$ above 200 K is probably due to the thermal radiation between the sample (and the assemblies) and the surrounding environment.

In Fig. 3(b), we present S_{xx} as a function of temperature. Similar to the resistance, both ferromagnetic transitions are reflected. Normally hole-type carriers give positive S_{xx} [39], but in Mn_3Sn_2 a sign change of S_{xx} at $T = 80$ K can be clearly seen, and the similar phenomenon was also observed for Mn_3Sn [21] and Fe_3Sn_2 [40]. The sign change likely arises from subtle changes in the band structure [41], leading to anomalies in carrier concentration, as discussed before. As a phenomenological explanation, we considered the contribution from hole diffusion (S_d), magnon drag (S_m), and phonon drag (S_p), with the former dominating at high temperatures and the latter two becoming significant at low temperatures. For a single parabolic band system, the S_d can be defined by the equation $\pi^2 k_\text{B}^2 T/3eE_\text{F}$ (k_B is the Boltzmann constant) [42]; additionally, $S_m \propto T^{3/2}$ [42] and $S_p \propto T^3$ [43] when the temperature is low enough. By linearly fitting the data above

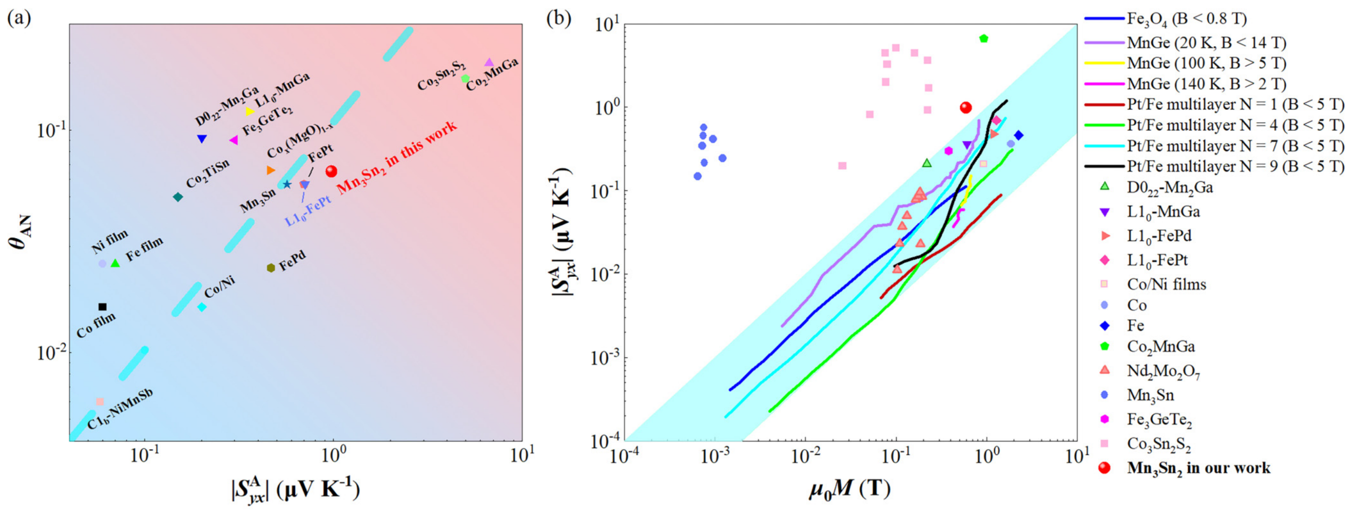

FIG. 4. (a) θ_{AN} vs $|S^A_{xy}|$ plot for Mn$_3$Sn$_2$ (at 200 K) and other reported anomalous Nernst materials. (b) Full logarithmic plot of the anomalous Nernst signal $|S^A_{xy}|$ versus the magnetization $\mu_0 M$ for a variety of metals and Mn$_3$Sn$_2$ (at 200 K). The shaded region indicates the linear relation for conventional ferromagnetic metals with $|N^A_{xy}|$ ranging $0.05 - 1$ μV K^{-1}T^{-1}. Except for Mn$_3$Sn$_2$, the other data were taken from Refs. [7,8,19,31,45–47].

100 K, we obtain a slope of 0.12 μV K^{-2}, corresponding to $E_F = 0.2$ eV. For the low temperature region, by fitting the data up to 60 K with the equation

$$S_{xx}(T) = AT + BT^{3/2} + CT^3, \tag{10}$$

we obtain coefficients $A = 0.0204$ μV K^{-2}, $B = -0.0237$ μV K$^{-2.5}$, $C = 3.7 \times 10^{-5}$ μV K^{-4} with $B \gg C$. This implies that magnon drag significantly contributes to S_{xx} at low temperatures, while phonon drag is negligible. Hence, magnetic excitation at low temperatures may be responsible for alterations in the bands near E_F, leading to subsequent changes in carrier concentration and Seebeck coefficients.

The magnetic field dependent Seebeck (Nernst) coefficients are determined through the symmetrization (antisymmetrization) of the thermoelectric voltages measured separately in the presence of positive and negative fields. The variation of $S_{xx}(\mu_0 H)$ with magnetic field at each temperature is small, as shown in Fig. S2 of the Supplemental Material [44]. Below T_N, a rapid decrease is observed in $|S_{xx}(\mu_0 H)|$ at low field ranges, similar to the behavior of magnetoresistance induced by magnetism.

As shown in Fig. 3(c), for all temperatures, the Nernst signal exhibits a rapid increase at low magnetic fields, with a subsequent additional increase attributed to the ordinary Nernst signal contribution. Following a similar procedure used for the Hall effect, we extracted the ordinary and anomalous contributions to the Nernst thermopower. The Nernst coefficient shows a jump of ∼1 μV K^{-1} around 200 K, and the corresponding anomalous Nernst angle ($\theta_{AN} = S^A_{xy}/S_{xx}$) is approximately 6.5%. Both values are relatively large compared to most materials exhibiting anomalous Nernst effects, as shown in Fig. 4(a). It is noteworthy that S_{xx} approaches zero as T decreases to ∼80 K, therefore θ_{AN} approaches infinity, as depicted in the inset in Fig. 3(c). Analogous to the AHE, the ANE of conventional ferromagnets is proportional to the magnetization, that is, $S^A_{xy} = N^A_{xy}\mu_0 M$, where N^A_{xy} is the anomalous Nernst coefficient. Illustrated in Fig. 3(d), N^A_{xy} of Mn$_3$Sn$_2$ reaches 1.65 μV K^{-1} T^{-1}, surpassing the values observed in conventional itinerant ferromagnets such as Fe, Co, and Ni (∼0.1 μV K^{-1} T^{-1}) [45] and exceeding the range typical for ferromagnetic metals (usually smaller than 1 μV K^{-1} T^{-1}) [4]. In Fig. 4(b), the anomalous Nernst signal of Mn$_3$Sn$_2$ is juxtaposed with the values of various metals and falls outside the shaded region of the linear scaling relation for conventional ferromagnetic metals. The observation is consistent with Mn$_3$Sn [46], Co$_3$Sn$_2$S$_2$ [47], and Co$_2$MnGa [8], indicating that the anomalous Nernst effect in Mn$_3$Sn$_2$ may stem from topological nontrivial energy band structures.

IV. CONCLUSION

In conclusion, we have observed an abnormal temperature dependence resistance, and large AHE and ANE in the ferromagnetic Mn$_3$Sn$_2$ single crystals. The occurrence of resistance maximum at Curie temperature T_{C2} and its negative temperature dependence above T_{C2} are closely related to a large spin-fluctuation scattering in the paramagnetic state. The anomalous Hall signal reaches ∼7 μΩ cm at 200 K and conforms to the scaling of $\sigma^A_{xy} \propto M$ and $\rho^A_{xy} \propto \rho^2_{xx}$ below 200 K. The ANE up to ∼1 μV K^{-1} at 200 K and a corresponding anomalous Nernst angle of ∼6.5% are both observed. Despite the large effective magnetic moment of Mn$_3$Sn$_2$, its anomalous Nernst coefficient falls outside the shaded region of the linear scaling relation typical for conventional ferromagnetic metals. Our results suggest the existence of a sizable nonzero Berry curvature near the Fermi level. Clearly, there is a need for more theoretical calculations and experimental measurements, such as angle-resolved photoemission spectroscopy, to examine the topological nature of Mn$_3$Sn$_2$.

ACKNOWLEDGMENTS

This work was supported by the National Natural Science Foundation of China (Grant No. 12274440), the Strategic

Priority Research Program (B) of Chinese Academy of Sciences (Grant No. XDB33010100), the Ministry of Science and Technology of China (Grant No. 2022YFA1403903), and the Synergetic Extreme Condition User Facility (SECUF).

J.B. and Q.D. contributed equally to this work.

[1] E. H. Hall, XXXVIII. On the new action of magnetism on a permanent electric current, London Edinburgh Philos. Mag. J. Sci. **10**, 301 (1880).

[2] N. Nagaosa, J. Sinova, S. Onoda, A. H. Macdonald, and N. P. Ong, Anomalous Hall effect, Rev. Mod. Phys. **82**, 1539 (2010).

[3] Y. Sakuraba, K. Hasegawa, M. Mizuguchi, T. Kubota, S. Mizukami, T. Miyazaki, and K. Takanashi, Anomalous nernst effect in $L1_0-$FePt/MnGa thermopiles for new thermoelectric applications, Appl. Phys. Express **6**, 033003 (2013).

[4] M. Mizuguchi and S. Nakatsuji, Energy-harvesting materials based on the anomalous Nernst effect, Sci. Technol. Adv. Mater. **20**, 262 (2019).

[5] D. Xiao, Y. Yao, Z. Fang, and Q. Niu, Berry-Phase effect in anomalous thermoelectric transport, Phys. Rev. Lett. **97**, 026603 (2006).

[6] I. Samathrakis, T. Long, Z. Zhang, H. K. Singh, and H. Zhang, Enhanced anomalous Nernst effects in ferromagnetic materials driven by Weyl nodes, J. Phys. D: Appl. Phys. **55**, 074003 (2022).

[7] S. N. Guin *et al.*, Zero-Field nernst effect in a ferromagnetic Kagome-lattice Weyl-semimetal $Co_3Sn_2S_2$, Adv. Mater. **31**, 1806622 (2019).

[8] S. N. Guin *et al.*, Anomalous Nernst effect beyond the magnetization scaling relation in the ferromagnetic Heusler compound Co_2MnGa, NPG Asia Mater. **11**, 16 (2019).

[9] S. Nakatsuji, N. Kiyohara, and T. Higo, Large anomalous Hall effect in a non-collinear antiferromagnet at room temperature, Nature (London) **527**, 212 (2015).

[10] Y. Machida, S. Nakatsuji, S. Onoda, T. Tayama, and T. Sakakibara, Time-reversal symmetry breaking and spontaneous Hall effect without magnetic dipole order, Nature (London) **463**, 210 (2010).

[11] D. Xiao, M.-C. Chang, and Q. Niu, Berry phase effects on electronic properties, Rev. Mod. Phys. **82**, 1959 (2010).

[12] J. Bai *et al.*, Highly anisotropic magnetism and nearly isotropic magnetocaloric effect in Mn_3Sn_2 single crystals, Chin. Phys. Lett. **40**, 127501 (2023).

[13] T. Mazet, H. Ihou-Mouko, and B. Malaman, Mn_3Sn_2: A promising material for magnetic refrigeration, Appl. Phys. Lett. **89**, 022503 (2006).

[14] F. Tang and X. Wan, Complete classification of band nodal structures and massless excitations, Phys. Rev. B **105**, 155156 (2022).

[15] K. Manna *et al.*, From colossal to zero: Controlling the anomalous Hall effect in magnetic Heusler compounds via berry curvature design, Phys. Rev. X **8**, 041045 (2018).

[16] J. Noky, J. Gooth, C. Felser, and Y. Sun, Characterization of topological band structures away from the Fermi level by the anomalous Nernst effect, Phys. Rev. B **98**, 241106 (2018).

[17] J. Noky, Q. Xu, C. Felser, and Y. Sun, Large anomalous Hall and Nernst effects from nodal line symmetry breaking in Fe_2MnX (X = P, As, Sb), Phys. Rev. B **99**, 165117 (2019).

[18] E. Liu *et al.*, Giant anomalous Hall effect in a ferromagnetic Kagome-Lattice semimetal, Nat. Phys. **14**, 1125 (2018).

[19] J. Xu, W. A. Phelan, and C.-L. Chien, Large anomalous nernst effect in a Van der Waals ferromagnet Fe_3GeTe_2, Nano Lett. **19**, 8250 (2019).

[20] T. Chen *et al.*, Large anomalous Nernst effect and nodal plane in an iron-based Kagome ferromagnet, Sci. Adv. **8**, eabk1480 (2022).

[21] X. Li, L. Xu, L. Ding, J. Wang, M. Shen, X. Lu, Z. Zhu, and K. Behnia, Anomalous nernst and Righi-Leduc effects in Mn_3Sn: Berry curvature and entropy flow, Phys. Rev. Lett. **119**, 056601 (2017).

[22] O. Gunnarsson, M. Calandra, and J. E. Han, Colloquium: Saturation of electrical resistivity, Rev. Mod. Phys. **75**, 1085 (2003).

[23] D. Cvijović, The Bloch-Gruneisen function of arbitrary order and its series representations, Theor. Math. Phys. **166**, 37 (2011).

[24] A. H. Wilson, The electrical conductivity of the transition metals, Proc. R. Soc. London, Ser. A **167**, 580 (1938).

[25] S. N. Kaul, Anomalous Hall effect in nickel and nickel-rich nickel-copper alloys, Phys. Rev. B **20**, 5122 (1979).

[26] *The Hall Effect and its Applications*, edited by C. L. Chien and C. R. Westgate (Plenum Press, New York, 1980).

[27] T. Miyasato, N. Abe, T. Fujii, A. Asamitsu, S. Onoda, Y. Onose, N. Nagaosa, and Y. Tokura, Crossover behavior of the anomalous Hall effect and anomalous nernst effect in itinerant ferromagnets, Phys. Rev. Lett. **99**, 086602 (2007).

[28] Q. Wang, S. Sun, X. Zhang, F. Pang, and H. Lei, Anomalous Hall effect in a ferromagnetic Fe_3Sn_2 single crystal with a geometrically frustrated Fe bilayer kagome lattice, Phys. Rev. B **94**, 075135 (2016).

[29] M. Huang *et al.*, Colossal Anomalous Hall Effect in Ferromagnetic van der Waals $CrTe_2$, ACS Nano **15**, 9759 (2021).

[30] Q. Wang, Z. Wen, T. Kubota, T. Seki, and K. Takanashi, Structural-order dependence of anomalous Hall effect in Co_2MnGa topological semimetal thin films, Appl. Phys. Lett. **115**, 252401 (2019).

[31] J. Hu *et al.*, Anomalous hall and nernst effects in Co_2TiSn and $Co_2Ti_{0.6}V_{0.4}Sn$ Heusler thin films, Phys. Rev. Appl. **10**, 044037 (2018).

[32] Y. Wang, C. Xian, J. Wang, B. Liu, L. Ling, L. Zhang, L. Cao, Z. Qu, and Y. Xiong, Anisotropic anomalous Hall effect in triangular itinerant ferromagnet Fe_3GeTe_2, Phys. Rev. B **96**, 134428 (2017).

[33] Y. Q. Zhang, N. Y. Sun, R. Shan, J. W. Zhang, S. M. Zhou, Z. Shi, and G. Y. Guo, Anomalous Hall effect in epitaxial permalloy thin films, J. Appl. Phys. **114**, 163714 (2013).

[34] J. Moritz, B. Rodmacq, S. Auffret, and B. Dieny, Extraordinary Hall effect in thin magnetic films and its potential for sensors, memories and magnetic logic applications, J. Phys. D: Appl. Phys. **41**, 135001 (2008).

[35] S. Onoda, N. Sugimoto, and N. Nagaosa, Intrinsic versus extrinsic anomalous Hall effect in ferromagnets, Phys. Rev. Lett. **97**, 126602 (2006).

[36] R. Mathieu, A. Asamitsu, K. Takahashi, H. Yamada, M. Kawasaki, Z. Fang, N. Nagaosa, and Y. Tokura, Anomalous Hall effect in Ca-doped $SrRuO_3$ films, J. Magn. Magn. Mater. **272-276**, E785 (2004).

[37] J. Yang, Theory of thermal conductivity, in *Thermal Conductivity: Theory, Properties, and Applications*, edited by T. M. Tritt (Springer, Boston, 2004), pp. 1–20.

[38] M. Jonson and G. D. Mahan, Mott's formula for the thermopower and the Wiedemann-Franz law, Phys. Rev. B **21**, 4223 (1980).

[39] H. J. Goldsmid, *Introduction to Thermoelectricity* (Springer, Berlin, Heidelberg, 2016), Vol. 121.

[40] Q. Du, M. G. Han, Y. Liu, W. Ren, Y. Zhu, and C. Petrovic, Room-temperature Skyrmion thermopower in Fe_3Sn_2, Adv. Quantum Technol. **3**, 2000058 (2020).

[41] J. Mao, Z. Liu, J. Zhou, H. Zhu, Q. Zhang, G. Chen, and Z. Ren, Advances in thermoelectrics, Adv. Phys. **67**, 69 (2018).

[42] S. J. Watzman, R. A. Duine, Y. Tserkovnyak, S. R. Boona, H. Jin, A. Prakash, Y. Zheng, and J. P. Heremans, Magnon-drag thermopower and Nernst coefficient in Fe, Co, and Ni, Phys. Rev. B **94**, 144407 (2016).

[43] M. Bailyn, Phonon-drag part of the thermoelectric power in metals, Phys. Rev. **157**, 480 (1967).

[44] See Supplemental Material at http://link.aps.org/supplemental/10.1103/PhysRevB.109.125112 for more detailed data on the magnetic field-dependent Hall effect, magnetoresistance, thermal conductivity, Seebeck effect, and Nernst effect.

[45] T. C. Chuang, P. L. Su, P. H. Wu, and S. Y. Huang, Enhancement of the anomalous Nernst effect in ferromagnetic thin films, Phys. Rev. B **96**, 174406 (2017).

[46] M. Ikhlas, T. Tomita, T. Koretsune, M.-T. Suzuki, D. Nishio-Hamane, R. Arita, Y. Otani, and S. Nakatsuji, Large anomalous Nernst effect at room temperature in a chiral antiferromagnet, Nat. Phys. **13**, 1085 (2017).

[47] H. Yang *et al.*, Giant anomalous Nernst effect in the magnetic Weyl semimetal $Co_3Sn_2S_2$, Phys. Rev. Mater. **4**, 024202 (2020).